Chapter 1
Nanotechnology Pathways to Next-Generation Photovoltaics

Stephen M. Goodnick

Abstract In this book chapter, an overview is given of the latest advances and central challenges in photovoltaics research, and the role of nanotechnology in improving performance. Over the long term, nanotechnology is expected to enable improvements throughout the energy sector, but the most striking near- to midterm opportunities may be in lower-cost, higher-efficiency conversion of sunlight to electric power. Nanostructures in solar cells have multiple approaches by which they can improve photovoltaic performance: (1) new physical approaches in order to reach thermodynamic limits, (2) allow solar cells to more closely approximate their material-dependent thermodynamic limits, and (3) provide new routes for low-cost fabrication by self-assembly or design of new materials. We focus primarily on the first two approaches which have the goal of increasing efficiency. The limits of solar cell efficiencies are discussed, and several different approaches are described that circumvent long-held physical assumptions and lead beyond first- and second-generation solar cell technologies. The role of nanotechnology in specific cell technologies is reviewed, including its role in improving light-trapping and the light collection properties of solar cells, as well as dye-sensitized solar cells and perovskite solar cells, and recent advances in nanowire solar cells. Special emphasis is given on novel nanostructure-based devices based on advanced concepts such as hot-carrier cells, and multiexciton generation, which have the theoretical basis to realize high-efficiency energy conversion.

S. M. Goodnick (✉)
School of Electrical, Computer and Energy Engineering, Arizona State University, Tempe, AZ, USA
e-mail: stephen.goodnick@asu.edu

S. M. Goodnick et al. (eds.), *Semiconductor Nanotechnology*, Nanostructure Science and Technology, https://doi.org/10.1007/978-3-319-91896-9_1

1.1 Overview of Photovoltaics

1.1.1 History and Basic Principles

Photovoltaic energy conversion is the direct conversion of light into electrical energy, without any intermediate steps such as steam generation in the case of solar thermal systems, for example. While photovoltaics is primarily associated with the revolution in semiconductor electronics in the latter half of the twentieth century, the photovoltaic effect itself was developed in 1839 by Edmond Bequerel in electrochemical cells. Although proceeded by earlier work, the first practical photovoltaics devices utilizing the solar spectrum, or solar cells, were demonstrated in 1954 at Bell Laboratories and found its first commercial applications as lightweight and long lifetime power sources for extraterrestrial applications for the emerging space industry in the late 1950s. Since that time, photovoltaics has developed into the fastest-growing source of terrestrial renewable energy, with an installed global capacity of over 400 GWs peak energy in 2017, and a production cost per watt that has dropped from $75/W in the late 1970s, to $0.30/W today, an exponential decrease in cost that is analogous to Moore's law for microelectronics.

The basic principal of operation of a photovoltaic device is illustrated in Fig. 1.1, which illustrates a pn junction under optical excitation. The operation of a photovoltaic device is truly quantum mechanical in nature, as quanta of electromagnetic radiation (photons) excite electrons from the valence band (filled states or orbitals) to empty or unoccupied states in the conduction band across a bandgap characteristic of the semiconductor (1.12 eV in the case of Si at room temperature, the dominant

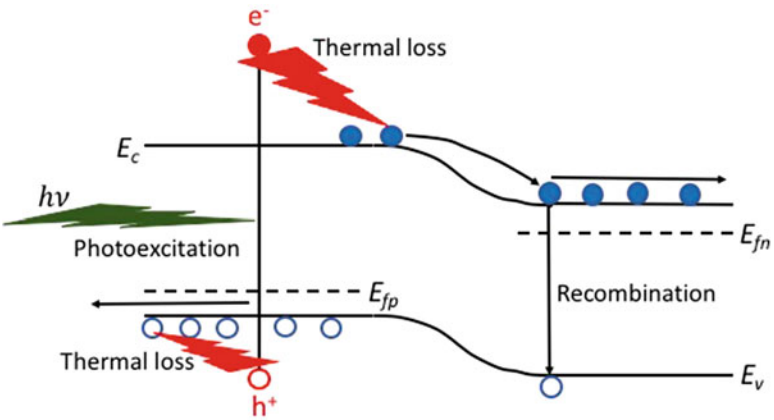

Fig. 1.1 Band diagram of a pn junction solar cell illustrating the generation, thermalization, and capture of photoexcited carriers

semiconductor material). Photons with energy $h\nu$ below the bandgap are not absorbed since there are no final states available, whereas photons with energy above the bandgap create *electron-hole pairs* as shown. The excess kinetic energy of these photoexcited electrons and holes lows their energy to the crystal lattice of the material through electron-phonon (quanta of vibrational energy) interactions on very short time scales (femtoseconds to picoseconds) and relaxes to the minimum energy of the conduction band for electrons and the maximum energy of the valence band for holes. What is critical in performing useful work with such excitations is to have a basic asymmetry in the system that separates the electron and hole, provided in this case of the pn junction in Fig. 1.1 by the *space charge region* between the p- and n-regions, and high electric field there, which accelerates electrons to the right, and holes to the left, where they are collected in their respective n- and p-regions, giving rise to a photocurrent.

Solar cells for both terrestrial and space applications are optimized with respect to the broadband nature of the solar spectrum, shown in Fig. 1.2. The sun may be modeled, to a high degree of accuracy, as a blackbody source with intensity given by

$$I(\lambda) = R_{sun}^2/D^2 \times \frac{2\pi hc^2}{\lambda^5\left(\exp\left(\frac{hc}{\lambda kT}\right) - 1\right)}, \tag{1.1}$$

where R_{sun} is the radius of the sun, D is the distance from the earth to the sun, T is the temperature of the sun, and λ is the wavelength; the rest of the fundamental constants have their usual meaning. As can be seen in Fig. 1.2, the solar spectrum at the top of the atmosphere is well fit with Eq. (1.1) using a temperature of 5250 C (the more

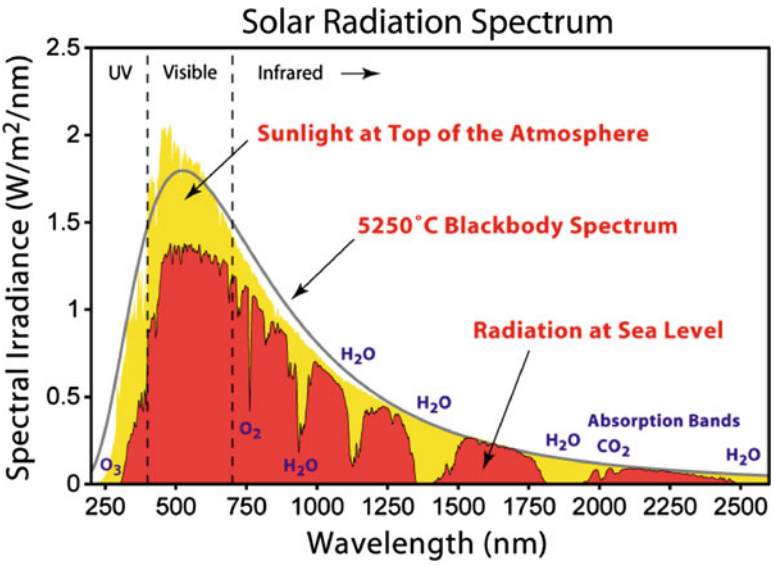

Fig. 1.2 Spectral irradiance versus wavelength for the solar spectrum at the top of the atmosphere and at the earth's surface compared with the ideal blackbody spectrum (Wikipedia commons)

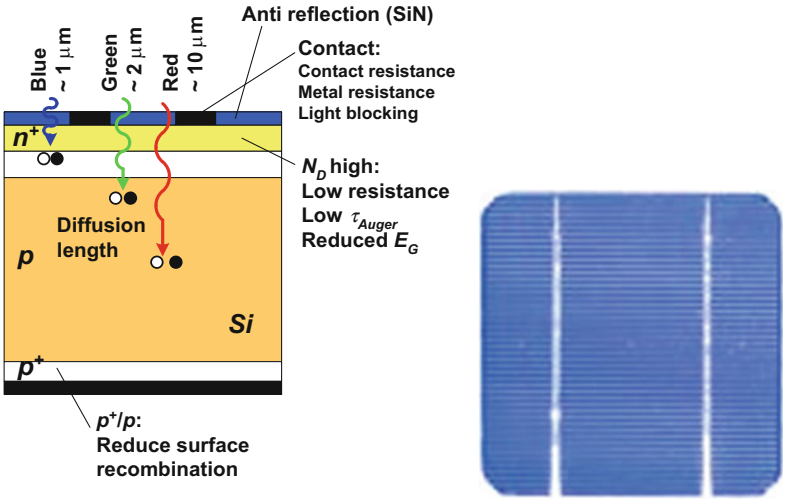

Fig. 1.3 Cross-sectional schematic of a generic Si solar cell (*left panel*) and a top view of a solar cell (*right*) showing the grid pattern for allowing light absorption and carrier collection

accepted value is 5762 K), whereas due to absorption and reflection losses from atmospheric constituents (water, CO_2, etc.), as well as diffuse Raleigh scattering, the solar spectrum on the earth's surface is reduced with loss bands and is a function of latitude where the atmospheric path length increases for higher latitudes, further reducing the intensity.

The design of a solar cell therefore has to take into account not only the photon energy and intensity of photons corresponding to the particular wavelength of light but also the absorption coefficient of the material at a given wavelength, which is the inverse of the mean absorption depth of photons. This is illustrated in Fig. 1.3 for a basic Si cell design, where longer wavelength red light has a relatively long absorption depth, whereas short-wavelength blue light is absorbed near the surface. The structure of a commercial Si solar cell device (Fig. 1.1) typically has a thick base region (here p-type), a narrow emitter layer that is highly doped to minimize lateral resistance, heavy doping near the back contact to reduce recombination of photogenerated electrons there (back surface field), and a grid top contact to the emitter which has narrow fingers to minimize optical reflection.

The photocurrent delivered by the solar cell to a resistive load results in a voltage drop which forward biases the pn junction diode of the cell, resulting in a "dark" current, I_D, that flows in the opposite direction as the photocurrent. This is illustrated in the equivalent circuit model for a solar cell shown in Fig. 1.4. The general form of this current for most junction devices is exponential

$$I_D = I_0\left(e^{qV_D/nkT} - 1\right), \tag{1.2}$$

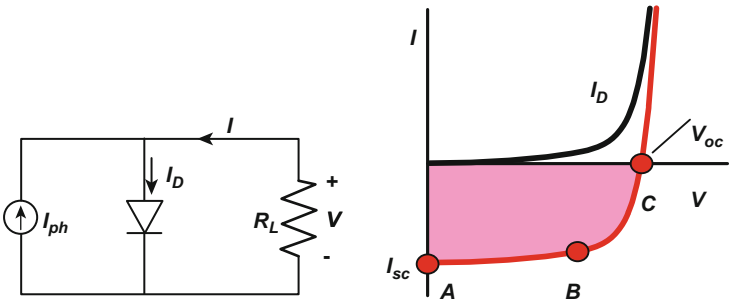

Fig. 1.4 Equivalent circuit of the solar cell and the corresponding current-voltage characteristics and important points along the I–V curve

where V_D is the voltage across the diode (which is different from V in Fig. 1.4 if series resistance is included), n is the ideality factor which varies between 1 and 2 usually, and I_0 is the reverse saturation current which depends explicitly on the recombination current in the junction, which can be radiative, due to traps or through Auger processes, and typically has an exponential dependence on the bandgap over the thermal voltage, i.e., $-E_g/kT$. As seen in terms of the net diode current, the I–V curve is shifted downward with light, corresponding to negative power or power generation. The points A, B, and C along the curve denote the short-circuit current, the maximum power point, and open circuit, three figures of merit for photovoltaic devices. The short-circuit current is usually the same as the photocurrent induced by light absorption, I_{ph}, and is proportional to the photon flux above the bandgap incident on the surface (correcting for reflection and transmission through the cell). The open-circuit voltage depends on the reverse saturation current, I_0, and hence the bandgap of the material. Under open-circuit conditions (infinite R_L), $I_D = I_0$, so that using Eq. (1.2)

$$V_{oc} = \frac{nkT}{q} \ln\left(\frac{I_{sc}}{I_o} + 1\right). \tag{1.3}$$

Since I_0 decreases exponentially with the bandgap, V_{oc} increases linearly with bangap, empirically given by $V_{oc} \approx E_G(in\ volts) - 0.4V$. Point B corresponds to the maximum power point and is decreased from the maximum potential power $I_{sc}V_{oc}$, due to the "roundness" of the I–V curve, the degree of which is termed the *fill factor* (FF). In terms of the total optical energy incident on the device area, P_{in}, the optical to electrical conversion efficiency, η, is given by

$$\eta = \frac{V_{oc} I_{sc} FF}{P_{in}} \tag{1.4}$$

1.1.2 Photovoltaic Technologies

The performance of various photovoltaic technologies in terms of their solar to electrical energy conversion efficiency has continuously improved in a monotonic fashion with time as shown in Fig. 1.5 in a plot published each year by the National Renewal Energy Laboratory (NREL). Silicon solar cell technology dominates the current world photovoltaic market, with 95% controlled by a combination of single-crystal and multicrystalline Si technologies at present [1]. The highest efficiency reported for single-gap Si device technology to date is 26.7% based on a heterojunction structure using as crystalline Si substrate with thin layers of amorphous Si (a-Si), which forms a heterojunction due to the larger bandgap of a-Si (~1.7 eV) [2]. This cell record was demonstrated on a large area device, with an interdigitated backside contact which eliminates the front grid pattern of Fig. 1.3, increasing the photocurrent. Heterojunction AlGaAs/GaAs single-crystal solar cells have achieved even higher performance of 28.8%, the highest for any single-bandgap device [3]. Due to the cost and availability of material, such III–V semiconductor solar cells are normally too expensive for normal flat-plate solar except for space applications, where efficiency and radiation resistance are considerations.

The technologies above are wafer based, being comprised of either a wafer of the underlying material as the base region of the device or starting with a wafer and then removing the active region by lift-off to make thin solar cells. Thin film technologies are ones in which the active regions of the device are deposited using various thin-film methods onto a low-cost support material, for example, metal or glass. Such materials traditionally have lower efficiency but lower fabrication and materials costs, thus achieving lower $/W cost. Initially, amorphous Si (a-Si) thin-film solar was the dominant thin-film technology but has since been supplanted by II–VI CdTe heterostructure technology, which as shown in Fig. 1.5 has demonstrated over 21% performance by First Solar [4] and is the basis for several large (>200 MW) utility-scale solar installations worldwide. Recently, chalcogenide-based materials such as CIGS ($CuInGaSe_2$) have demonstrated similar high efficiencies and have taken an increasingly larger market share.

Organic thin-film solar cells are conceptually similar to the thin-film solar cells in the preceding paragraph, in which organic semiconductor materials are deposited onto glass or other support materials, however, defined by their HOMO (highest unoccupied molecular orbital) and LUMO (lowest unoccupied molecular orbital) levels. Rather than n- and p-type materials and the formation of a homojunction with a corresponding space charge region, a heterojunction is formed in which the lineup of the HOMO-LUMO levels of two different materials (called donor and acceptor materials) forms the junction. Due to the strong excitonic binding energy of organic materials, the photoexcited electron and hole are strongly bound as excitons, and diffuse to the heterointerface, where they dissociate due to the asymmetry of the barrier there into separate free electrons and holes on either side of the heterojunction, which are then collected at the contacts giving rise to a photocurrent. Due to the short diffusion lengths of excitons in such materials, *blended*

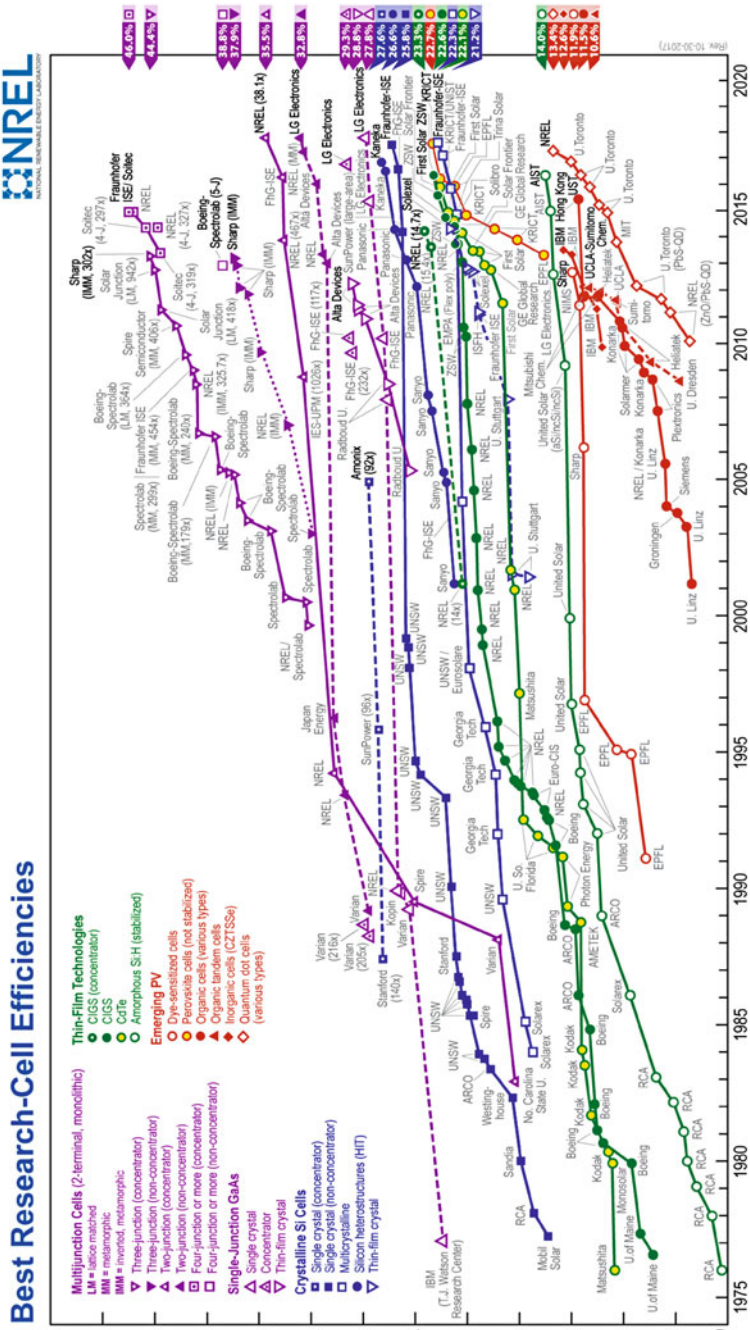

Fig. 1.5 Measured solar cell efficiency records for various technologies versus time (NREL https://www.nrel.gov/pv/)

heterostructures with the donor and accepter materials interdiffused into a network give better charge collection and performance. A common organic solar cell material combination is based on P3HT (poly(3-hexylthiophene)) which acts a donor material and PCBM (6,6-phenyl-C61butyric acid methyl ester) which acts as an acceptor material [5]. While efficiencies are generally lower than inorganic thin-film approaches, the fabrication process for organic is much less expensive, and organic layers can generally be spun on, not requiring vacuum deposition or high-temperature processing, although recent high-performance organic cells have moved in this direction [6].

Hybrid organic-inorganic perovskite materials have made remarkable advances in solar cell efficiencies over the past 5 years. These hybrid perovskite materials are of the general form ABX_3, which forms in the perovskite crystal structure, with the most commonly studied form being methylammonium lead iodide, $CH_3NH_3PbI_3$, with B=Pb, C=I, and the organic playing the role of the A component [7]. The bandgap of $CH_3NH_3PbI_3$ is 1.55 eV, which makes it suitable for terrestrial photovoltaics, and its transport properties are quite good compared to the typical organic materials discussed in the preceding paragraph, with electron and hole mobilities comparable to inorganic semiconductors, and diffusion lengths on the order of microns, with relatively weak excitonic effects. The original work on perovskite solar cells was based on a dye-sensitized solar cell architecture [8], which is a nanostructured device technology discussed more in Sect. 1.3.2, in which the hybrid perovskite is infused into a mesoporous wide-bandgap TiO_2 structure which acts as an electron acceptor from the perovskite, while holes are extracted in an electrolytic liquid cell structure. This efficiency was greatly improved by replacing the liquid electrolyte with a solid organic hole transport layer (spiro-MeOTAD), leading to the high efficiencies reported today in excess of 20%. A further innovation was the evolution of the mesoscopic structure to a planar structure in which $CH_3NH_3PbI_3$ is treated essentially as a polycrystalline semiconductor [9], although both approaches continue to be developed. As seen in Fig. 1.5, the performance of perovskite solar cells has one of the steepest slopes of any technology over a very short time period, reaching a record as of today of 22.7% at the Korean Research Institute of Chemical Technology (KRICT), surpassing that of thin-film inorganic technologies. The advantage of perovskite technology is the low manufacturing cost, comparable to something between organic and thin-film inorganic material and processing costs. The main barrier to commercialization to date are issues associated with the long-term stability due to the sensitivity of the perovskite to water vapor, which various groups are addressing through encapsulation and improved materials processing.

Finally, in the context of this brief review of commercial or near-term technologies, multijunction or tandem solar cells are the highest-efficiency technology presently, particularly at high concentration. In tandem solar technology, multiple bandgap junction devices are connected together or simply grown sequentially on a substrate, where the multiple bandgaps reduce the thermalization loss and transparency issues of a single-bandgap solar cell, as discussed in more detail in Sect. 1.2. The highest-efficiency tandem devices are single-crystal III–V materials grown epitaxially on top of one another, starting with the lowest-bandgap material, and

ending with the highest bandgap, in terms of the direction of the incident radiation. In this way, the short-wavelength light is absorbed in the top wide-bandgap material, and the longer-wavelength light is absorbed by subsequent layers. The cells are typically connected together in series with tunnel junctions, such that overall, the current is the same through all the cells, and the overall cell voltage is the sum of the voltages of the individual cells. The cost of the substrates and high-quality epitaxial growth (using, e.g., molecular beam epitaxy, or MBE) makes the cost per cell quite high. The high cost of these devices is compensated for by using them in an optical concentrator (where the light intensity is 200×–400× higher than typical sunlight), such that only very small areas are needed. The optical systems must track the sun, and these large systems are suited primarily for utility-scale applications. Three junction cells based on Ge/GaAs/GaInP or similar combinations have exceeded 40% efficiency as shown in Fig. 1.5, and the record as of the time of this writing is 46% from Fraunhofer ISE and Soitec at a concentration of 297×.

1.2 Limits of Efficiency

1.2.1 Detailed Balance Analysis

A photovoltaic device may be ideally analyzed independent of its material parameters (apart from bandgap) from thermodynamic considerations only, called *detailed balance*. Shockley and Queisser's 1961 paper [10] is based on an idealized description of a solar converter which includes no details of the cell structure itself; rather, it assumes complete collection of available photogenerated carriers with the following basic assumptions: (1) radiative recombination only, (2) one bandgap, (3) absorption across the bandgap in which one photon generates one electron-hole pair, (4) constant temperature in which the carrier temperature is equal to the lattice and ambient temperature, and (5) steady state, close to equilibrium. Mathematically, the current density is written in terms of three terms

$$J = qg\left[\left(fC\int_{E_G}^{\infty}\frac{E^2dE}{\exp\left(\frac{E}{kT_{sun}}\right)-1}+(1-fC)\int_{E_G}^{\infty}\frac{E^2dE}{\exp\left(\frac{E}{kT}\right)-1}\right)-\int_{E_G}^{\infty}\frac{E^2dE}{\exp\left(\frac{E-qV}{kT}\right)-1}\right], \tag{1.5}$$

with

$$g=\frac{2\pi}{h^3c^2}\quad f=\left(\frac{R_{sun}}{D_{sun}}\right)^2 \tag{1.6}$$

where C is the concentration factor, E_g is the material bandgap, and V is the voltage across the cell. Equation (1.5) is written in terms of blackbody sources of photons, in which the first term represents the incident photon flux from Eq. (1.1), with T_{sun} the

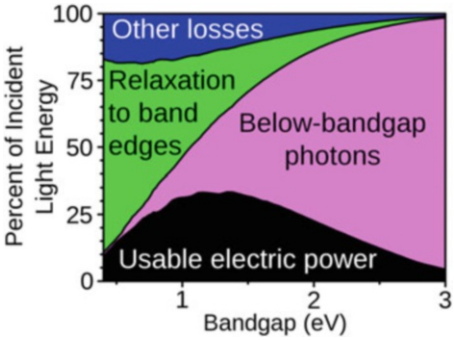

Fig. 1.6 The Shockley-Queisser efficiency limit (black curve) versus bandgap for the AM1.5 solar spectrum and the contributions to this limit due to different loss mechanisms (Source: Wikipedia Commons)

temperature of the sun, and the second term represents the blackbody radiation from the surroundings at the local ambient temperature, T. The third term represents the blackbody radiation re-radiated by the absorber which is out of equilibrium in terms of the voltage V, which represents the splitting of the quasi-Fermi energies within the material. If a solar spectrum other than the ideal blackbody spectrum is used, then the first term is replaced simply by the integral of the photon flux above the bandgap.

In Eq. (1.6), the "dark" current discussed in the previous section is only due to blackbody radiation from the semiconductor absorber, which in effect is due to radiative recombination within the semiconductor generating photons above the bandgap. By evaluating the integrals for a range of voltages going from zero to the bandgap, the maximum JV product is found, giving the conversion efficiency in terms of the total incident power. The result of this calculation is plotted in Fig. 1.6, where the black curve is the calculated efficiency versus bandgap for an AM1.5 terrestrial solar spectrum. The maximum efficiency without concentration is around 33.7% corresponding to maxima at 1.1 and 1.4 eV. The principal losses are due to the loss of photons with energy below the bandgap, and loss of the excess energy of the photon above the bandgap in terms of energy relaxation of photoexcited carriers back to the band edges, with thermalization being the main loss for small bandgap materials and optical transparency the main loss for high bandgaps.

1.2.2 Exceeding the Shockley-Queisser Limit

As discussed above, main factors contributing to Shockley-Queisser (SQ) limit in Fig. 1.6 are that photons below the bandgap of the absorber are not collected, while any excess kinetic energy in the electron-hole pair created by a photon above the bandgap is quickly lost through thermalization and therefore only contributes the energy an electron-hole pair at the bandgap, independent of the photon energy. The variation and limiting value then of the efficiency with bandgap is a direct result of the specific broadband nature of the solar spectrum, with a peak at 33.7%. In contrast, the theoretical limit of solar to electrical energy conversion has been considered by several authors based on thermodynamics alone and is approximately

85% [11], and therefore there is a substantial gap between the single-gap SQ limit and what should be possible.

There are various pathways to approaching thermodynamic conversion efficiencies rather than the single-gap SQ limit, by circumventing the assumptions inherent in the SQ analysis, which we discuss in more detail below.

Broadband Solar Spectrum As mentioned above the fact that the solar spectrum is a broad band source leads to the trade-offs between transparency to below bandgap photons and thermalization energy losses for those above. If the solar spectrum could be transformed to a narrower spectrum, higher-efficiency performance is possible. Up/down conversion of the solar spectrum through phosphors or two-photon absorption/emission are potential methods to accomplish this.

Multiple Electron-Hole Pairs per Photon The SQ analysis assumes a single electron-hole pair (EHP) excitation per photon, but the excess energy of the photon above the gap may be sufficient to produce a second or third, etc. EHP. Another route to exceeding the single-gap limit is to generate multiple electron-hole pairs from a single photon through the creation of secondary carriers. The process of impact ionization in semiconductors by high-energy charge carriers is well known, and the potential considered for photovoltaics [12]. More recently, nanostructured systems such as quantum dots and nanowires have shown particularly promising results due to quantum confinement effects, where the effect is often referred to as multiexciton generation (MEG), due to the importance of excitonic states in strongly confined systems, which we discuss in more detail in Sect. 1.3.5 [13].

Extraction of Hot Carriers Before Thermalization To circumvent the loss associated with thermalization (the loss of excess kinetic energy of photoexcited carriers), Ross and Nozik proposed the concept of hot-carrier solar cells [14]. In this concept, electrons and holes are not collected at the band edges (which limits to the output voltage to the bandgap), rather they are collected through energy-selective contacts above and below the conduction and valence band edges, respectively, effectively increasing the operating voltage. The absorber material suppresses energy loss, so that hot carriers can reach sufficient energy to escape through the energy-selective contacts. The concept was extended further by Würfel and coworkers who considered the effect of impact ionization and secondary carrier generation on the ultimate efficiency of this concept [15, 16]. Recent results are discussed in more detail later in Sect. 1.3.6.

Multiple Bandgaps/Energy Levels The SQ analysis considered only a single-gap material, but already in the mid-1950s, it was recognized that multijunction or tandem solar cells were capable of efficiencies above that of single-gap devices. Tandem solar cells have shown the highest efficiencies of any solar cell technology [17], with the record to date in excess of 46% in a four-junction structure [18], which greatly exceeds the single-gap SQ limit. The detailed balance approach given by Eq. (1.5) can be generalized to consider multiple junctions, each with its own detailed balance equation and with a modified spectrum according to the number of cells above or below (due to reabsorption of emitted light) the particular junction

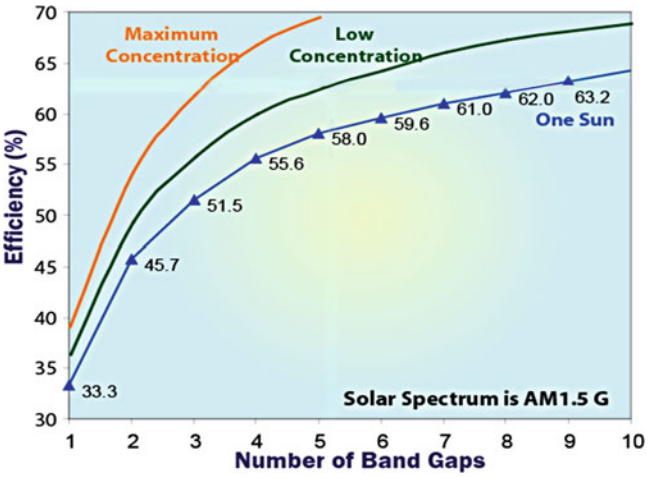

Fig. 1.7 Calculated detailed balance efficiency of as a function of the bandgap number for a tandem cell, for three different concentrations of AM1.5 spectrum sunlight

in question. The results of this calculation for different numbers of bandgaps for normal, low, and high concentration are shown in Fig. 1.7. Concentration provides a significant improvement in performance for high number of junctions, which can be explained simplistically in terms of Eq. (1.3) for the open-circuit voltage increase with photocurrent (proportional to concentration) and having junctions in series where the effect is additive, multiplying the concentration effect. For maximum concentration (set by étendue limits to 46,050X), one can approach the thermodynamic limit with an arbitrarily large number of junctions.

As discussed earlier, commercial tandem cells are grown in series using epitaxial material growth technology, which is generally quite expensive compared to conventional Si solar cell manufacturing and has many material challenges to both optimize the bandgaps and have lattice-matched materials for low-defect growth. There has been a recent revival in interest in Si tandem solar cells, e.g., increasing the efficiency of current Si technology with an additional junction grown on a Si substrate, to improve the performance without a substantial cost increase. For a 1.12 eV lower-bandgap material, the optimum bandgap for a top material is 1.7 eV. Based on lattice-matching considerations, GaP is one of the few that is nearly lattice matched to S and can be an alternative to a-Si as a heterojunction technology [19]. Its 2.36 eV bandgap is unsuitable for monolithic tandem applications, which has led to consideration of dilute nitride materials in order to match both bandgap and lattice constant [20].

Rather than fabricating multiple junctions, another approach is to introduce multiple levels within the same material, which provide multiple paths for photon absorption but collect carriers at the primary bandgap of the host material. Luque and Marti introduced the concept of an intermediate-band (IB) solar cell to realize such a structure and overcome the SQ limit [21], while similar concepts had been suggested

for quantum well solar cells. An intermediate level in the bandgap is introduced through, for example, self-assembled quantum dots, which allow low-energy photons to excite electron-hole pairs through multiphoton absorption, below the gap of the principal absorber.

1.3 Nanotechnology Pathways for Photovoltaics

Nanotechnology refers to technology at literally nanometer-scale dimensions (10^{-9} meters), although the term is used somewhat loosely for devices with critical feature sizes below 100 nm, which is a broad umbrella encompassing a host of scientific and engineering disciplines including life sciences, physics, chemistry, engineering, and computer science, among others. Nanotechnology has been driven by remarkable advances in materials synthesis, nanofabrication, and atomic-scale characterization over more than four decades. The nanotechnology and nanoscience fields represent a convergence of many different disciplines, partly driven by top-down miniaturization driven by Moore's law and the microelectronics industry and bottom-up approaches driving chemistry and the life sciences, where self-ordered nanoscale structures are naturally occurring and responsible for the exquisite functionality that exits in biomolecular structures. The ability to visualize and characterize atomic-scale features began with remarkable advances in high-resolution electron microscopy and lattice imaging and then invention of the scanning tunneling microscopy and atomic force microscopes [22], which allows atomic-level imaging of atomic positions, spectroscopic features, and positioning of atoms on a surface.

Top-down nanofabrication techniques such as electron-beam, ion-beam, and deep ultraviolet (UV) lithography allow the patterning of features down to 10s of nanometers, and AFM techniques can be used to actually position atoms literally with atomic precision. At the same time, there have been significant advances in "bottom-up" synthesis and control of self-assembled materials such as nanoparticles, nanowires, molecular wires, and novel states of carbon such as fullerenes, graphene, carbon nanotubes, and composites thereof. These advances have led to an explosion of scientific breakthroughs in studying the unique electronic/optical/mechanical properties of these new classes of materials.

Nanostructures in solar cells have multiple approaches by which they can improve photovoltaic performance: (1) new physical approaches in order to reach thermodynamic limits, (2) allow solar cells to more closely approximate their material-dependent thermodynamic limits, and (3) provide new routes for low-cost fabrication by self-assembly or design of new materials. Some of the specific advantages and disadvantages presented by nanotechnology are listed below:

Advantages

- Range of bulk materials with proper energy gaps, catalytic properties, etc. very limited: Nanostructured materials allow "bandgap engineering" of electronic states and energy gaps: artificial materials.
- Provide intermediate energy centers within host material.
- Optical absorption can be increased; reflection and other optical losses decreased.
- Improve transport and reduce scattering and energy loss.

Disadvantages

- Higher surface-to-volume ratio means surface effects dominate: higher recombination.

In the following, we first summarize what the important nanomaterial technologies consist of in terms of nanoparticle, nanowires, and quantum wells. This is followed by consideration of different nanotechnology-based solar cell architectures such as dye-sensitized solar cells, and nanowire solar cells, as well as a discussion of light management in photovoltaic devices through nanostructures. We then end considering two advanced concept technologies including multiexciton generation devices and hot-carrier solar cells, followed by a summary.

1.3.1 Nanomaterials

Nanomaterials usually refers to materials that have structural features on the nanoscale and in particular their properties stem from these nanoscale dimensions. Such nanomaterials may include quantum wells, nanoparticles, nanopowders, nanoshells, nanowires, nanorods, nanotubes such as carbon nanotubes, nanomembranes, and nanocoatings or combinations of these to form nanocomposites. An important feature of nanomaterials for energy applications compared to their bulk counterparts is that the surface-to-volume ratio is greatly enhanced, resulting in fundamental changes in the chemical, electronic, mechanical, and optical properties, in essence creating a new material. Such changes are a result of the different energies associated with surfaces compared to the bulk. This may result in complete changes in the way materials may behave, in terms of their catalytic properties, their chemical bonding, strength, etc. Another effect is the so-called quantum size effect, which, like the simple particle in a box, quantizes the motion of electrons in a solid, meaning the allowed energies can only assume certain discrete values. This generally changes the electrical and optical properties of materials. For example, nanoparticles show a blue shift in their absorption spectrum to high frequency due to quantum confinement effects.

Quantum Wells and Superlattices

One of the first truly nanoscale fabrication technologies was the development of precision epitaxial material growth techniques such as molecular beam epitaxy (MBE) [23] and metal-organic chemical vapor deposition (MOCVD), through which high-quality, lattice-matched heterojunction (junction between two dissimilar materials) semiconductor-layered systems could be realized, with atomic precision in the interface quality. A sandwich composed of a narrower bandgap material clad with larger bandgap materials of atomic dimensions is referred to as a quantum well (QW), and when many of these are grown sequentially, they are referred to as a multi-quantum well (MQW) system. These systems exhibit strong quantum confinement effects due to the low density of defects at the interface of lattice-matched materials such as GaAs and $Al_xGa_{1-x}As$. If the thickness of the barriers separating large and small bandgap materials is reduced so that the electronic states of the QWs overlap, the system is referred to as a superlattice (SL), which behaves as a new material electronically.

The capability of epitaxial growth to realize atomically precise heterointerfaces has served as the basis for a number of electronic and optoelectronic device technologies including heterojunction bipolar transistors (HBTs), high-electron mobility transistors (HEMTs), quantum well lasers, quantum well infrared photodetectors (QWIPs), and quantum cascade lasers (QCLs), to mention a few. In photovoltaic applications, single-crystal epitaxial growth is the basis for high-efficiency tandem or multijunction solar cells which hold the record for conversion efficiency as discussed earlier. They typically are designed for high-performance extraterrestrial applications (space-craft) or high-performance terrestrial concentrating photovoltaic (CPV) applications. MQW systems are also of active interest for QW solar cells or several of the advanced concept devices discussed in the next section.

Nanowires

The term *nanowire* generally refers to a high aspect ratio wire-like structures in which the cross-sectional dimensions are nanometer scale, while the length may be micro- to macroscale. Nanowires are generally solid, not hollow structures, the latter being referred to as *nanotubes*. Such nanowires may be oxide, metallic, or semiconducting. One of the major broad techniques used for the growth of semiconducting nanowires is *vapor-phase synthesis*, in which nanowires are grown by starting from appropriate gaseous components. In the so-called *vapor-liquid-solid* (VLS) mechanism, which uses metallic nanoparticles as seed sites to stimulate the self-assembled growth of nanowires. The desired semiconductor system is introduced in terms of its gaseous components, and the entire assembly is heated to a temperature beyond the eutectic temperature of the metal/semiconductor system. Under these conditions, the metal forms a liquid droplet, with a typical size of a few nanometers. Once this droplet becomes supersaturated with semiconductor, it essentially nucleates the

growth of the nanowire from the base of the droplet. Figure 1.6 shows examples of Si nanowires grown by VLS method using gold nanoparticles as the seeding droplets. The high-crystalline integrity of this nanowire can be clearly seen in this image, which also makes clear how the diameter of the nanowire is connected the size of the catalyst droplet [24]. The wire shown here was grown by using chemical vapor deposition (CVD) to generate the semiconductor precursors, a popular approach to VLS. Other methods may also be used, however, including laser ablation and MBE. The VLS method has emerged as an extremely popular method for the fabrication of a variety of nanowires. It has also been used to realize various III–V (GaN, GaAs, GaP, InP, InAs) and II–IV (ZnS, ZnSe, CdS, CdSe) semiconductor nanowires, as well as several different wide-bandgap oxides (ZnO, MgO, SiO_2, CdO).

Samuelsson and coworkers have also had enormous success in developing nanoscale electronic devices that utilize VLS-formed, III–V semiconductor, nanowires as their active elements [25]. They have demonstrated that heterostructure nanowires of InAs and InP, as well as GaAs and InAs, can be realized that have very sharp heterointerfaces [26]. They have subsequently used this technique to implement a variety of nanoscale devices, such as resonant-tunneling diodes [27] and single- [28] and multiple-coupled [29, 30] quantum dots. The strong lateral confinement generated in these structures, combined with their high-crystalline quality, endows them with robust quantum-transport characteristics. Quantum dots realized using these structures show very clear single-electron tunneling signatures, with evidence that the g-factor of the electrons can be tuned over a very wide range [31]. The ability to arbitrarily introduce serial heterointerfaces into such nanowires should offer huge potential in the future for the further development of novel nanodevices (Fig. 1.8).

From the perspective of energy conversion, nanowire structures are being researched as new materials for electrochemical storage and energy conversion devices, due to the large surface-to-volume ratio of these structures, which improves

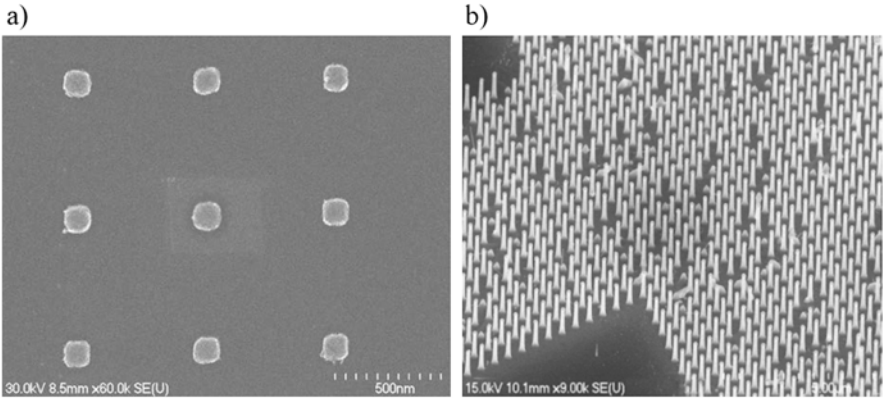

Fig. 1.8 Self-assembled growth of nanowires using vapor-liquid-solid (VLS) epitaxy. (**a**) Scanning electron micrograph of Au seeds patterned with electron-beam lithography. (**b**) Ge nanowires after growth on Si (111) [32]

the catalytic performance and reaction rates, as well as provides large internal surface areas for charge storage. Within renewable energy technologies such as solar photovoltaic devices, nanowires are finding increasing use in light management, reducing the amount of light lost and allowing less material to be used for the absorption of light, hence improving efficiency and lowering material cost. Most of these efforts are in the research phase or as part of start-up ventures commercially.

Nanoparticles and Quantum Dots

Nanoparticles is a name generally given to ultrafine size particles with dimensions on the order of 1–100 nm. If the nanoparticles are single-crystal individual particles, they are often referred to as nanocrystals [33]. Alternately, agglomerates of nanoparticles are referred to as nanopowders. Nanoparticles can be metals, dielectrics, or semiconductors. They can also be grown with different compositions to form core-shell nanoparticles with unique electrical and optical properties, as illustrated in Fig. 1.7. Their electronic and optical properties are different from bulk materials as mentioned before due to quantum size effects which shift the fundamental gap to higher energy. Surface effects also play a dominant role. In particular, the dielectric properties can also be modified by surface plasma resonance effects, which change the absorption properties. The high surface-to-volume ratio affects other properties such as diffusion properties in liquid and the adhesive properties.

Nanoparticles are synthesized by a variety of techniques. One inexpensive method is through ball mill micro-machining to literally grind materials down into nanoparticles. Pyrolysis and rf plasma techniques may also be used. A popular method for synthesizing nanoparticles of high quality is through chemical solution methods; in particular sol-gel methods can realize colloidal solutions of nanoparticles which may be subsequently dried for individual nanoparticles, or the gel solutions cast for particular applications. Another method of realizing semiconductor nanoparticles is through self-assembly of InAs or InGaAs quantum dots that on a GaAs substrate via the Stransky-Krastinov growth process [34]. In this mode of growth, a thin layer of InAs is grown on top of a GaAs substrate, but, if the layer is sufficiently thin, the strain will cause the InAs to agglomerate into small three-dimensional quantum dots.

Nanoparticles (and other nanomaterials such as nanowires and nanotubes) can be embedded in a host matrix to form a *nanocomposite*. The main differentiating factor between a nanocomposite and a normal composite material is the large surface-to-volume ratio of the nanoparticle, which means that there is a large internal surface area associated with the nanoparticles compared to normal composite materials. Therefore, a much smaller amount of nanoparticle composition can have a much greater effect on the overall nanocomposite properties. Nanocomposites can be comprised of many forms, the primary ones be ceramic matrix, metal matrix, or polymer matrix nanocomposites (Fig. 1.9).

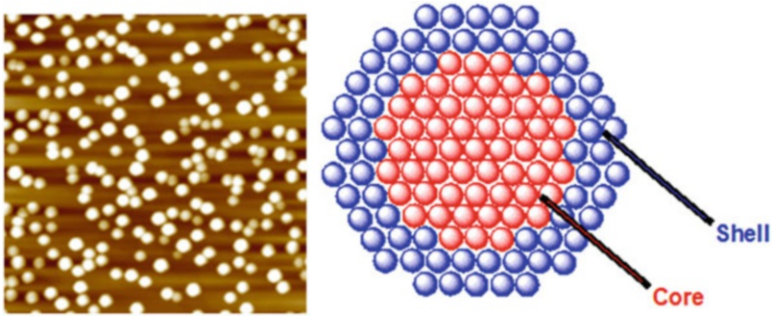

Fig. 1.9 Micrograph of self-assembled InAs nanoparticles on a GaAs substrate (left) [35] and a schematic of a core-shell nanoparticle (wiki commons)

1.3.2 Dye-Sensitized Solar Cells

Dye-sensitized solar cells (DSSC) are based on an electrochemical cell structure harkening back to Becquerel's experiments in the 1800s, which first demonstrated the photovoltaic effect. The DSSC was first realistically demonstrated by O-Regan and Grätzel in 1991 [36] and by its construction can be considered one of the first applications of nanotechnology to solar cells. Since this first demonstration, traditional DSSC efficiencies have reached over 11%. They have since been superseded by perovskite solar cell technology, as discussed in Sect. 1.1.2, as the first perovskite solar cells evolved from the DSSC architecture, and the highest efficiency perovskite cells still incorporate a nanostructured DSSC-like structure.

A schematic of a typical DSSC architecture is shown in Fig. 1.10. It consists of nanoparticle or nanostructured TiO_2, which is a wide-bandgap material (E_g=3.2 eV). It is usually formed on a glass substrate with a transparent conducting oxide (TCO) such as indium tin oxide (ITO) or fluorine-doped tin oxide (FTO), which is the side light enters. A dye material such as a ruthenium (Ru) is introduced through, for example, a liquid spin-on coat and dry process, which adheres the dye to the TiO_2 nanostructure, to realize large surface area coverage. The HOMO-LUMO separation of the dye is matched to the solar spectrum, and when light is absorbed by the dye, the excited e^- transfers to TiO_2 as shown, due to the lineup of the conduction band of the TiO_2 relative LUMO level of the dye. The electron quickly diffuses to the TCO and the external circuit. The positive charge in the HOMO level reacts via a redox couple in the electrolyte; a typical electrolyte in DSSC cells is iodine based, consisting of I^- and I_3^-. The dye is reduced and the iodine oxidized by a process in which $3I^- = 2e^- + I_3^-$, that is, two holes in the dye are neutralized by converting three iodine ions into one I_3^- singly charged molecule, giving up to electrons to the dye. At cathode, the positive charge carrier, I_3^- is reduced and converted back to $3I^-$ by the transfer of two electrons from the cathode, thus completing the circuit.

The improvement in efficiency over time of DSSCs initially increased rapidly and then plateaued somewhat as seen in Fig. 1.5. Some of the limitations of the liquid

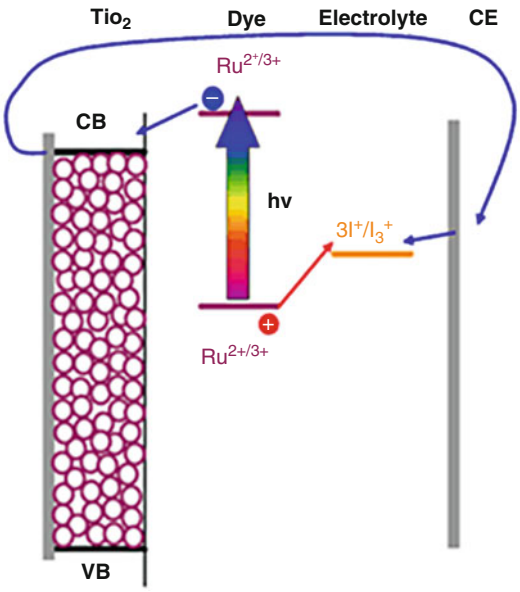

Fig. 1.10 Schematic of dye-sensitized solar cell (DSSC) architectures (wiki commons)

electrolyte approach to DSSC have included stability issues associated with the liquid electrolyte itself, the relatively narrow spectral absorption in the dyes, and low open-circuit voltages to recombination processes such as at the dye-TiO_2 interface. Improvements in finding new dye materials including inorganic nanoparticles with broad absorption and improvements in the structure to reduce recombination processes have led to performance improvements in recent years.

The most dramatic evolution of the DSSC architecture was, as discussed earlier, the replacement of conventional dyes with the hybrid perovskite $CH_3NH_3PbI_3$, which is a semiconductor material with a bandgap of 1.55 eV and could be introduced into the nanoporous TiO_2 matrix through low-temperature processing. Further, the liquid electrolyte was replaced by a solid organic hole-transport layer (spiro-MeOTAD) with good transport properties, leading to a much more compact planer geometry similar to conventional solar cells. In fact, purely planar structures without the requirement of nanostructured TiO_2 have been demonstrated with efficiencies approaching those of nanostructured cells [9]. At the time of this review, however, the highest record efficiencies still are those associated with the nanostructured approach with origins in the DSSC architecture [37].

1.3.3 Nanostructures for Improved Optical Performance

In order to approach or surpass the SQ limit of efficiency, all the available photons above the bandgap need to be absorbed and collected. Light management in solar cells focuses on the former, that of absorbing all the photons available. Absorption in

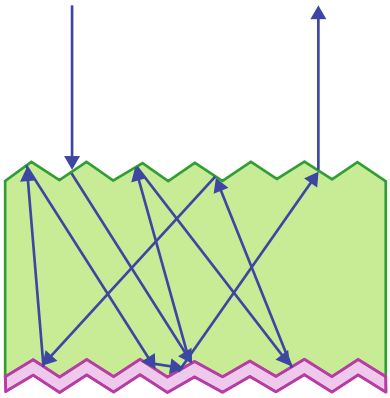

Fig. 1.11 Illustration of the classical path of light in a general semiconductor absorber structure including texturing of the front, the back, and a back reflector

semiconductors is primarily based on the absorption coefficient, $\alpha(h\upsilon)$, which is roughly the inverse of the absorption depth in a material. It is a strong function of wavelength, starting from zero at the band edge (ideally), and for shorter wavelengths, increasing in value, so that for very short wavelengths approaching the ultraviolet, the absorption depth may be just a few tens of nanometers. The fraction of photons absorbed at a given wavelength may be written as

$$f = [1 - R(\lambda)]\left(1 - e^{-\alpha(\lambda)l}\right) \tag{1.7}$$

where R is the reflection coefficient from the front surface and l is the path length of photons in the semiconductor before exiting. There are two main factors to optimize: one is to minimize the reflectance loss from the front of the device, and the second is to maximize the αl product such that the second term is close to zero. Part of the light management strategy with respect to nanostructuring is to minimize reflectance, while another part is concerned with increasing the effective optical path length and effective absorption coefficient.

Consider the geometry shown in Fig. 1.7 of a general absorber, which in general has a backside reflector and textured front and back surfaces. What is shown is the classical trajectory of a light ray incident on the surface (and not reflected), as it passes through the absorber and out again. If the width of the absorber is W, for a smooth surface, with no back reflector, $l = W$, and with perfect reflection, $l = 2\ W$ (assuming perfect transmission out the front surface) (Fig. 1.11).

In the case of a material with surface and back texturing, we see that the ray is scattered randomly and may make multiple passes through the material. Using statistical arguments based on diffusive scattering from the surfaces and ray optics, the limit to which the effective path length through the material may be enhanced is limited by the so-called classical light-trapping limit [38]

$$\langle l \rangle = 4n_s^2 W \tag{1.8}$$

where n_s is the index of refraction of the semiconductor. For example, in the case of Si, for red light, $n_s \approx 3.8$, which means the maximum enhancement of the path length is about 60 times.

For materials like Si which is an indirect bandgap materials, the absorption coefficient is relatively small for long-wavelength photons, requiring more than 200 microns or more of material to capture photons (not to mention long diffusion lengths to capture the photogenerated carriers), which add to the material cost as well as performance. Organic materials also suffer from poor absorption for long-wavelength photons. So much of the focus in terms of light management is on this longer-wavelength portion of the spectrum.

Nanostructured materials offer the potential to go beyond the classical light-trapping limit with feature sizes that are smaller than the characteristic wavelengths of light, and hence being in a regime of diffraction-limited optics. One interesting case is when we have periodic arrays of scatterers which coherently interact to produce *photonic bandgap* materials [39, 40]. Just as in the quantum picture of solids that the periodic potential of the crystal lattice modifies the free-electron dispersion and opens up energy gaps, likewise a periodic array of dielectric scatterings has the same effect on the optical dispersion, creating "bandgaps" in the optical spectra, creating passbands and stopbands for various ranges of frequencies. Such arrays can then be used to reflect or selectively enhance absorption in certain ranges of frequencies, allowing one to exceed the classical light-trapping limit.

Figure 1.12 shows an example of the measured reflectance from Si nanopillars fabricated using nanosphere lithography, in which silica nanoparticles are dispersed in a close-packed structure on the surface of Si and then regularly spaced nanopillars formed using reactive ion etching through the nanospheres [41]. The result is shown in the micrograph on the left side of the picture. The right side shows the measured reflectance (dashed curves) from a bare Si surface compared with two different

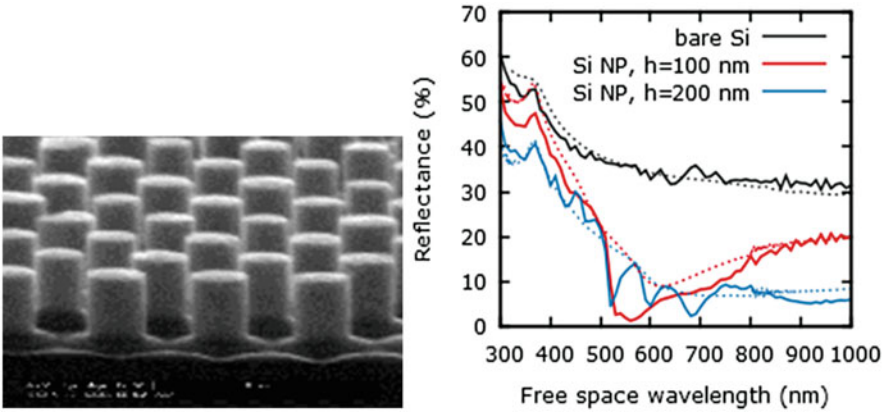

Fig. 1.12 Left: Micrograph of nanosphere lithographically defined nanopillars. Right: FDTD simulated (solid) and measured (dashed) reflectance spectra from a regular hexagonal array of Si NPs with period, $p = 600$ nm, for cylinder heights of 100 (red) and 200 nm (blue) [34]

nanopillar heights and the numerical simulation using full-wave finite-difference time-domain (FDTD) simulation of the scattering electromagnetic waves. As can be seen, the nanopillars significantly decrease the reflectance due to light trapping and that this reflectance is well described by the full-wave electromagnetic solutions to Maxwell's equations (as opposed to ray optics). The additional features in the numerical simulation are due to the sharp features assumed in the simulated geometry as opposed to smoothing of the pillars due to the etching process. A systematic study of different nanowire arrays in terms of periodic versus random in terms of the absorption of photons has demonstrated the possibility of exceeding the classical light-trapping limit in Eq. (1.8) over a limited band of optical frequencies [42].

A plasmonic structure for solar cells consists of nanoparticles on a surface or interface, typically consisting of small metal nanoparticles (Au, Ag, Al, Cu, etc.). Here surface photonic modes (polaritons, which are quasiparticles formed by the strong interaction between an EM wave and dipoles excitations in the solid like optical phonons) are coupled with charge oscillations in the metal nanoparticles (plasmons) to form what are called surface plasmon polariton modes. In particular, the nanoparticles have strong dispersion in the vicinity of the plasma frequency of the metal electrons, and incident light can strongly couple to these resonant modes, and are strong scattering along the surface, increasing the absorption and effective optical path length. The plasmonic structure may be introduced on the top surface, bottom surface, or within the active volume of the solar cell to increase absorption. Plasmonics has been investigated in both Si and III–V solar cells, as well as organic cells, demonstrating increased light trapping in the infrared regions. For Si solar cells, for example, path length enhancements of 7–8 times have been reported [43]. Plasmonic nanoparticle arrays on GaAs cells showed increase in short-circuit current of 8% [44].

1.3.4 Nanowire Solar Cells

Nanowire (NW) solar cells are a good example of nanotechnology applied to photovoltaics, illustrating several of the advantages discussed earlier and while at the same time addressing some of the disadvantages by mitigating recombination issue at surfaces. Nanowire-based solar cells have emerged in recent years as promising candidates for next-generation solar cells [45–48]. One of the advantages of NWs is the ability to tailor the bandgap through the geometry and composition of the NW, providing the ability to match the electronic and optical absorption properties during growth to the desired application, which bulk materials cannot do. In particular, due to their high aspect ratio and small cross sections, NWs can alleviate stress along their sidewall surfaces without forming detrimental lattice-mismatch-related defects, such as threading dislocations that form in planar epitaxial growth beyond a critical thickness. This property of NWs makes it possible to grow nanowire arrays on substrates with large lattice mismatch, as well as grow NW heterojunctions of highly lattice-mismatched materials, which would not be possible

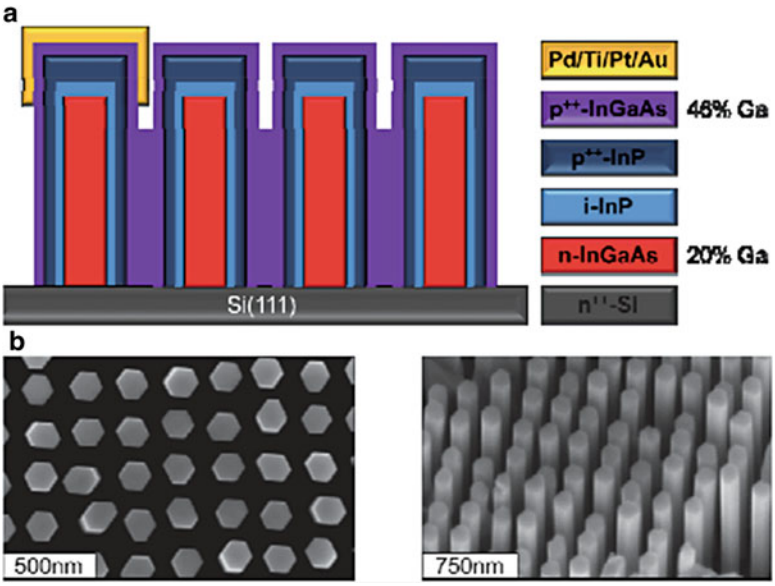

Fig. 1.13 (**a**) Schematic of InGaAs core-shell nanowire solar cells and (**b**) SEM picture of a fabricated array [50]

in planar structures. At the same time, as discussed in the preceding section, arrays of NWs strongly modify the optical properties of the system due to the photonic bandgap materials where the NWs can be thought of as "antennas" which strongly localize optical modes and lead to greatly enhanced absorption. As such, arrays of NWs provide strong optical absorption with a fraction of the material volume required in a bulk absorber.

Until now the best performance in NW solar cells have been demonstrated in III–V compound semiconductors like GaAs, due to the large absorption coefficient and excellent transport properties of the III–Vs. However, the requirement of III–V substrates makes them very expensive, where, as discussed earlier, the main application is restricted to space applications of solar cells. On the other hand, III–V nanowire arrays can be grown on cheap substrates opening the path for novel devices. A schematic of an InGaAs NW array solar cell architecture is shown in Fig. 1.13. The particular geometry shown is based on a radial core-shell design used for other optoelectronic applications by Treu et al. [49]. Almost all NW solar cells are fabricated by growing vertical arrays of NWs patterned top down, in the particular case of Fig. 1.13, using nanoimprint lithography, which is relatively inexpensive for nanopatterning. The challenge is to make contact to the n- and p-regions of the device. One strategy is to fill in the regions between the NWs with a spin-on insulator like PDMS (polydimethylsiloxane) and then to contact the tips of the NWs with a conducting oxide like ITO. The scheme shown below contacts the p^{++} outer shell InP with a thin cap of p^{++} InGaAs which connects the cells in parallel,

which are then contacted by a gold-alloy finger structure (the n-contact is made to the doped Si) (Fig. 1.13).

The growth of III–V nanowires on Si for optoelectronic applications was reported in 2010 by Chuang et al. [51] when they presented the first GaAs nanowire light-emitting diode (LED) and GaAs nanowire avalanche photodetector (APD) grown on a silicon substrate with growth conditions compatible to CMOS technology. One year later the same group produced the first InGaAs/GaAs core-shell NW laser grown on silicon [52]. This work demonstrated the hybrid integration of III–V semiconductor nanowires on silicon chips, with huge potential that has only recently begun to be exploited.

In relation to nanowire-based solar cells, two main designs are employed as discussed earlier: radial, core-shell junction and the axial junction devices, either p-n or p-i-n. In the case of core-shell NWS, Colombo et al. reported single GaAs nanowire p-i-n NW solar cells [53] with an efficiency of 4.5% and a good V_{oc} for GaAs cells of almost 1 V. The same group more recently reported single-nanowire solar cells with the potential to exceed the Shockley-Queisser limit [54]. Besides single-nanowire SCs, nanowire arrays are the subject of intense research. Radial GaAs junction arrays have been demonstrated by Mariani et al. [55] with efficiencies of 2.54% and high reproducibility. State-of-the-art axial InP p-i-n junction arrays have reached a record 13.8% efficiency as shown by Borgström et al. [56]. Sol Voltaics and Lund University reported GaAs VLS-grown nanowire solar cells with 15.3% efficiencies which were independently verified [57]. More recently, Eindoven University reported a 17.8% InP vertical junction nanowire solar cell formed by etching and passivation [58]. As can be seen, the improvement in NW solar cell technology has rapidly evolved, from a few percent in 2009 to over 17% in 2017, not dissimilar to the rapid improvement of perovskite solar cells, although surprisingly the technology does not appear on the NREL efficiency charts (Fig. 1.5) at present.

1.3.5 Multiexciton Generation

Figure 1.14 illustrates the creation of multiple electron-hole pairs for different photon energies, assuming simplistically that all the excess energy goes into the electron kinetic energy in the conduction band. As can be seen, there are different thresholds reached in energy when the photon energy in this picture is $h\nu = 2E_g$, $3E_g$, $4E_g$, etc., resulting in 2EHPs, 3EHPs, etc. As we discuss below from detailed balance, increasing the quantum efficiency above 100% through multiple EHP creation allows one to exceed the SQ limit of a single-gap system.

Generation of multiple electron-hole pairs has been known in bulk materials since the 1960s in Ge and demonstrated experimentally in bulk silicon solar cells [11]. However, impact ionization or Auger generation processes have a low efficiency in bulk materials and too high a threshold energy for effective utilization of the solar spectrum due to crystal momentum conservation. Nanostructured materials have been shown experimentally to increase the efficiency of carrier multiplication

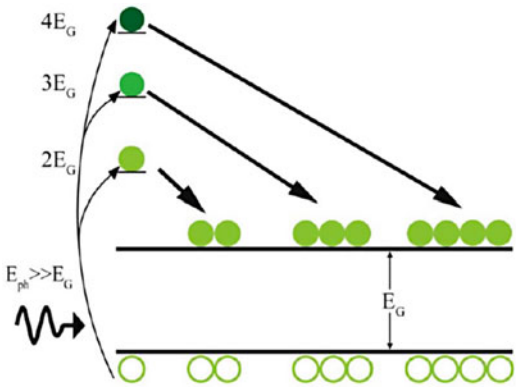

Fig. 1.14 Illustration of the multiexciton generation process for $M = 1, 2, 3,$ and 4

processes, with lower thresholds for carrier multiplication, and experimental demonstration of multiple exciton generation (MEG) in materials such as PbSe and PbS colloidal quantum dots [59, 60] with quantum efficiencies well in excess of 300%. The improved performance in nanocrystals over bulk systems is due to the relaxation of crystal momentum conservation in quantum dots, which, in bulk systems together with energy conservation, make the threshold for carrier multiplication roughly a factor of 1.5 higher than the bandgap. Due to quantum confinement, crystal momentum is no longer a good quantum number, and the threshold for carrier multiplication occurs at roughly multiples of the bandgap itself. Recent experimental evidence [61], as well as theoretical calculations [62], suggests indeed that the multi-excitation of several electron-hole pairs by single photons in quantum-dot structures occurs at ultrashort time scales, without the necessity of impact ionization. Overall, MEG generation has been shown in multiple materials, including PbSe, PbS, InAs [63], PbTe [64], Si [65], and CdSe [66].

The increase in the efficiency of a solar cell due to MEG processes may be calculated using the detailed balance approach of Eq. (1.5), by multiplying the integrand of the first integral corresponding to the incident photon flux by a quantum efficiency, $Q(E)$, representing the number of EHPs per photon generated due to impact ionization of multiexciton generation. For the case in which all the kinetic energy of the photon appears in the conduction band, we can write this mathematically as

$$Q(E) = \sum_{m=1}^{M} m\Theta(E - mE_g) \tag{1.9}$$

where Q is the quantum efficiency, m is the number of electron-hole pairs generated by a photon, E_g is the threshold energy (which is ideally equal to the bandgap energy), M is the maximum number of electron-hole pairs generated per an incident photon, and Θ represents the unit step function. Assuming a blackbody spectrum

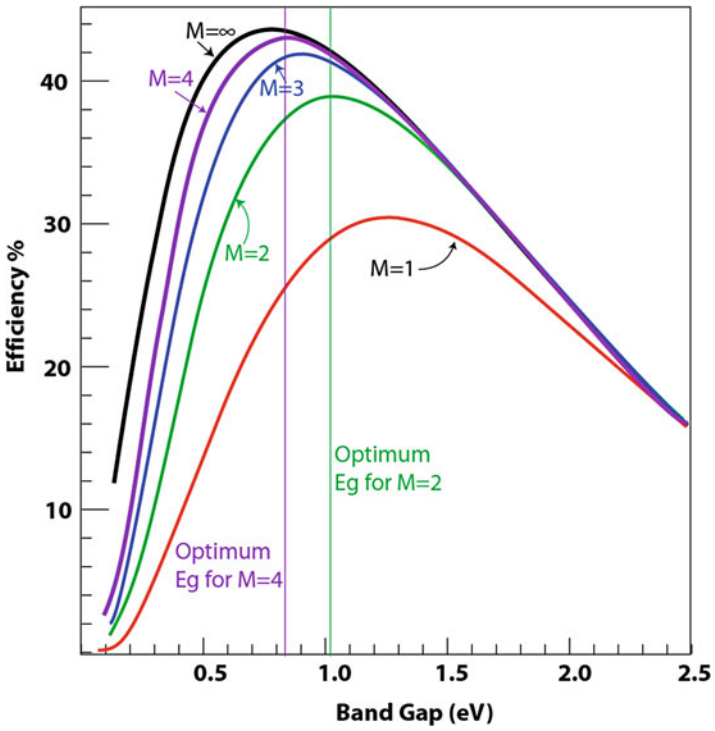

Fig. 1.15 Calculated detailed balance efficiency as a function of bandgap for the AM0 blackbody spectrum with consideration of increasingly higher-order multiplication factors

(the result is similar of the AM1.5 spectrum), the result of detailed balance using the quantum efficiency of Eq. (1.9) is given in Fig. 1.15.

The optimum bandgap for a completely ideal MEG device is 0.76 eV [67] for M going to infinity, whereas for M limited to 2, the optimum bandgap is 1.05 eV, very close to that of Si. However, ideal quantum efficiency given by the step function of Eq. (1.9) assumes the existence of multiple separate, non-interacting MEG generation processes, i.e., the band structure must be ideal for generating two excitons, as well as for three excitons, and so on, and also assumes that each of these MEG processes does not interact. Further, due to the high energies involved, the photon energy is more evenly split between electrons in the conduction band and holes in the valence band, leading to a smearing out of the sharp threshold for successive MEG events.

Experimentally, the quantum yield measured using ultrafast spectroscopy shows a threshold higher than $2E_g$, with a finite slope as shown in the quantum yield data from NREL [59] shown in Fig. 1.16. As can be seen, the quantum yield in bulk Si is relatively low with a threshold voltage beyond 3.5 eV, whereas for Si nanoparticle, the threshold is much lower and the slope steeper. More recently, PbSe quantum-dot

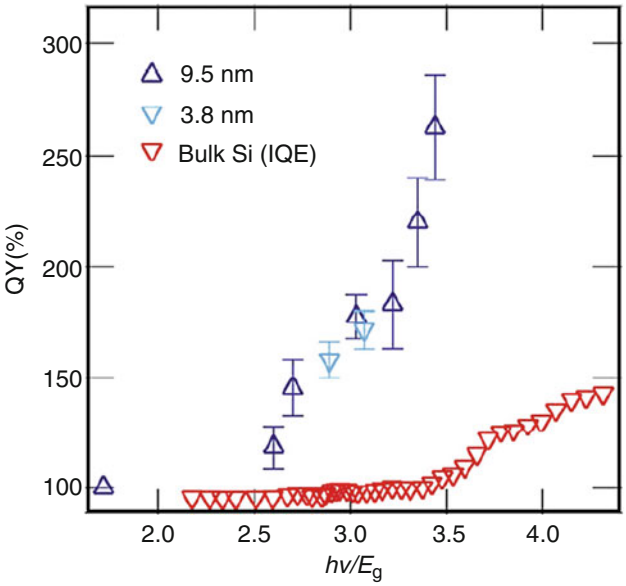

Fig. 1.16 Measured quantum yield versus photon energy (normalized by the bandgap) for bulk Si and two different diameters of nanoparticles. (Reprinted with permission from Beard et al. [66]. Copyright 2007 American Chemical Society)

solar cells were reported in which for short wavelengths, quantum efficiencies (correct for reflection) greater than 100% were measured [68].

Multiexciton generation has been measured more recently in PbSe nanowire/nanorod structures [69], where the threshold for enhanced quantum yield was lower than that of nanoparticles of the same material. This result is quite promising, as nanowires allow transport long the axis of the nanowire, allowing efficient collection of the generated EHPs, in contrast to nanoparticles, which generally require some sort of tunneling process to extract carriers.

In terms of multiexciton generation, there is competition between the impact excitation process (assuming that it is an incoherent process) and other energy relaxation mechanisms such as electron-phonon scattering, which is responsible for thermalization, one of the two major losses discussed earlier responsible for the single-gap SQ limit. The trade-offs between phonon scattering and impact ionization in narrow nanowires (1–5 nm) have been investigated theoretically using ensemble Monte Carlo simulation, a particle-based technique for simulating the nonequilibrium dynamics of photoexcited electrons and holes [70]. Figure 1.17 shows the calculated scattering rates based on the electronic states in the nanowire from an atomistic sp3d5s* tight-binding representation. What are shown are the bulk versus nanowire rates for deformation potential scattering (energy averaged) and polar optical phonon scattering, the two major lattice relaxation processes in III–V materials. As can be seen, the nanowire rates at low energy deviate strongly due to the highly 1D nature of the electronic states, whereas at high energies, the nanowire

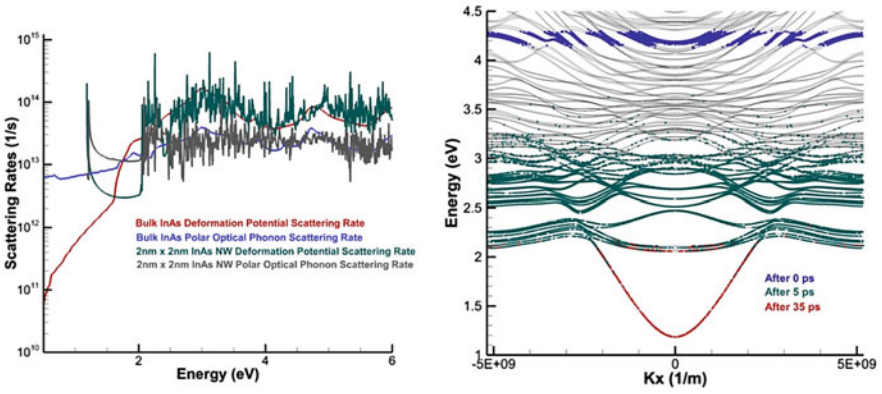

Fig. 1.17 Calculated scattering rates in 2 nm InAs NWs compared to the bulk scattering rates for deformation potential scattering and polar optical scattering (left panel). The simulated relaxation with the NW band structure for different snapshots in time starting with a high-energy nonequilibrium distribution [70]

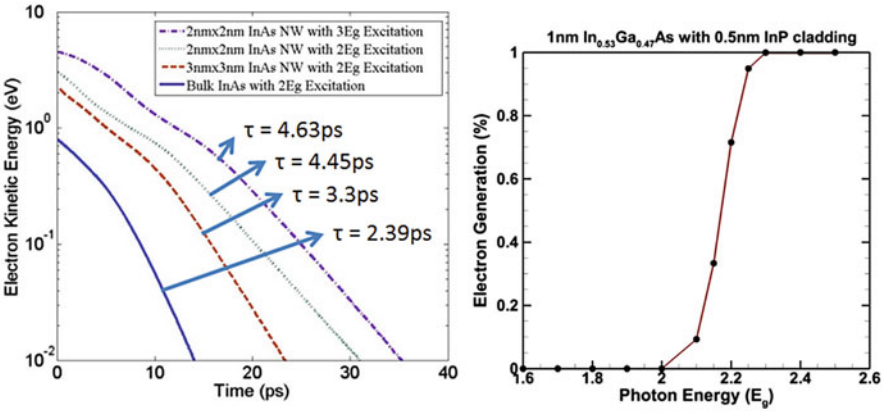

Fig. 1.18 Average energy versus time for a $2E_g$ excitation of carriers in the conduction band of different size nanowires versus bulk (left panel). Corresponding simulated quantum yield versus excitation energy

bands merge together to approximate the bulk density of states, and hence the same corresponding scattering rates. The right panel of Fig. 1.17 shows snapshots at various times of the time evolution of a nonequilibrium carrier distribution due to high-energy photoexcitation, which shows that as carriers relax, a bottleneck occurs in going to the ground state due to the energy separation and reduced scattering rates, leading to longer energy relaxation.

In Fig. 1.18, the average electron kinetic energy of photoexcited carriers in the conduction band of the InAs NW as a function of time for different nanowire dimensions compared with the bulk rate is shown on the right side. As can be

seen, the energy loss rate is substantially reduced in the NW system, almost double that of bulk InAs, and increases for increasingly smaller NWs. The corresponding electron generation due to impact excitation is shown on the rate, showing that at nearly $2E_g$, there is a strong threshold for carrier generation, which indicates that NWs should be good candidates for MEG-based solar cells.

1.3.6 Hot-Carrier Solar Cells

Ross and Nozik proposed the concept of hot-carrier solar cells [71] more than 25 years ago as a means to circumvent the limitations imposed by the Shockley-Queisser limit in terms of both the loss of excess kinetic energy and the loss of sub-bandgap photons. Figure 1.19 shows a schematic of the basic concept. The ideal absorber represents a material with a bandgap, $E_G \geq 0$, across which electron-hole pairs are excited by photons with energies greater than E_G. In the absorber, the relaxation of excess kinetic energy to the environment (i.e., the lattice) is suppressed, while the carriers themselves still interact strongly to establish a thermalized distribution, such that the electrons (and holes) are characterized by an effective temperature, T_H, much greater than the lattice temperature, T_L. This carrier temperature can be so large as to reverse the net chemical potential difference, μ_{ch}, between electrons and holes, and typically must be on the order of several thousand degrees for efficient operation.

Energy-selective contacts are made to the absorber on the left and right, where the left contact extracts hot electrons in a narrow range of energies above the conduction band edge as shown, while the contact on the right extracts holes (injects electrons) at a specific energy range in the valence band. In this scheme, the electrons and hole are extracted from the system before they have time to relax their excess energy, hence utilizing the total energy of the photon. Under the assumption of no energy loss, the maximum efficiency occurs for vanishingly small bandgaps, hence capturing photons over the entire solar spectrum. In this limit, the theoretical detailed balance conversion efficiency approaches the maximum thermodynamic conversion efficiency of 85.4% [72]. Later, Würfel and coworkers considered the effect of

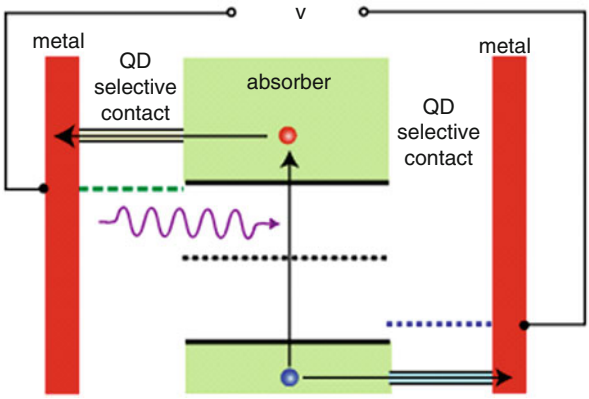

Fig. 1.19 Schematic of a hot-carrier solar cell consisting of an ideal absorber with energy-selective contacts

impact ionization and secondary carrier generation on the ultimate efficiency of this concept [73, 74].

There are many practical limitations to implementing this very ideal structure. One difficulty is realizing energy-selective contacts. Würfel pointed out [53] that it is necessary to spatially separate the absorber material for the cold metallic contacts themselves, which may serve as an energy loss mechanism to the carriers in the absorber layer. There it was suggested that a large bandgap material such as GaN serves as a spacer or "membrane" separating the absorber from the contacts. Other proposals for energy-selective contacts include using nanostructured resonant tunneling contacts from double-barrier heterostructures, defects, or artificial quantum dots [75].

The main challenge in the technology is to realize an ideal absorber in which the excess kinetic energy of the photoexcited carriers is not lost to the environment. There have been various proposals for reducing the carrier cooling rate. Due to the reduced dimensionality and therefore reduced density of final states in nanostructured systems, the energy loss rate due to phonons may be reduced, which has been observed experimentally [76]. In particular, in nanostructured systems such as quantum wells, quantum wires, or quantum dots, where intersubband spacing between levels is less than the optical phonon energy, then the optical emission rate may be suppressed due to the so-called "phonon bottleneck" effect, since there is no final states for the electron. However, even in such systems, the reduced phonon emission rate is still too fast for sufficient carrier heating, even under high solar concentration. As we saw in the previous section on energy relaxation in NWs, the energy loss rate is reduced by a factor of two compared to bulk, although this rate is still too fast of establishing a steady-state hot-carrier distribution in the absorber.

If, however, the energy is retained in the coupled electron-phonon system, then the energy may be recycled through hot-phonon reabsorption. Nonequilibrium hot-phonon effects during ultrafast photoexcitation have been well studied for many years. Time-resolved Raman scattering has been used, for example, to characterize the optical phonon decay after photoexcitation for a variety of III–V compound bulk and quantum well materials [77–80]. Ensemble Monte (EMC) simulation has previously been used to theoretically model ultrafast carrier relaxation and hot-phonons effects in quantum well and bulk materials [81, 82], where hot phonons have been shown to significantly reduce the rate of carrier cooling compared to the bare energy loss rate.

Figure 1.20 shows the results of ensemble Monte Carlo simulation of a quasi-2D system (10 nm GaAs/AlGaAs quantum well) of the early-stage carrier relaxation dynamics. The simulation includes both optical phonon (polar and deformation potential) and carrier-carrier scattering (electron-electron, hole-hole, electron-hole) and illustrates several effects. In the left panel, we see the early athermal carrier distribution that is more or less Gaussian shaped around the injection energy. A secondary peak already appears, which is an optical phonon replica of the main peak due to the short emission time. For longer times approaching a picosecond, electron-electron scattering drives the athermal distribution toward a heated Fermi-Dirac distribution, which is at a different temperature than the lattice, and over a

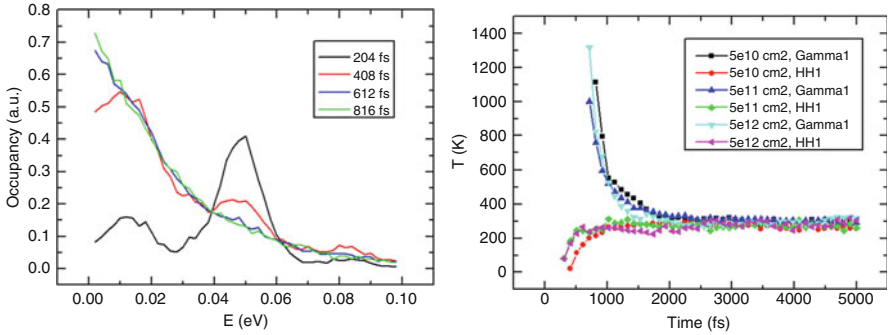

Fig. 1.20 Left panel: Ensemble Monte Carlo simulation of the ultrafast electron dynamics in the conduction band of a 10 nm GaAs quantum well at 300 K for carriers injected at 50 meV above the band edge, with an injected carrier density of $5\times10^{11}/\text{cm}^2$. Right panel: Electron and hole temperatures versus time after ultrafast carrier excitation for different injected carrier densities

much longer time scale (see, e.g., Fig. 1.18). The right panel shows the evolution of the electron and hole temperatures (taken from the average energy), where initially the electron and hole average temperatures are very different. However, over a period of 2 ps, the two temperatures reach a common temperature due to electron-hole scattering, which exchanges energy between the two systems.

Basically the main energy relaxation channel for electrons is through optical phonons, which lose energy through optical phonon emission in quanta of the optical phonon energy. However, due to the small group velocity of optical phonons, they do not leave the excitation volume; rather they must decay into acoustic phonons through a three-phonon anharmonic scattering process, and it is the acoustic phonons which propagate energy away from the active region of the device. Hence electrons and holes may reabsorb the excess phonons, and so the excess kinetic energy of the photoexcited EHPs remains in the system until the optical phonons decay to acoustic modes. It has been argued by the UNSW group that nonequilibrium "hot" phonons may play a critical role in reducing carrier energy loss and maintaining energy within the absorber [83]. Typical optical phonon decay times range from 1 to 10 ps, much longer than the electron-optical phonon emission rate (which is subpicosecond in scale). Engineering materials as absorbers with long phonon decays, particularly nanoengineered structures, are currently being investigated [56].

Figure 1.21 shows the simulated effect of phonon lifetime on carrier relaxation using EMC simulation, similar to earlier work on this topic [60, 84]. Here a 2 eV laser pulse exciting a 10 nm GaAs/AlAs QW is simulated, which peaks at 1 ps into the simulation, and is 200 fs wide. Optical absorption is modeled by creating electron-hole pairs corresponding to photons with a given frequency and momentum. Figure 1.21 plots the carrier temperature as a function of time for various assumed phonon lifetimes ranging from 0 (i.e., no hot phonons) to 100 ps.

As can be seen in the simulated results of Fig. 1.21, without hot phonons, the electrons cool rapidly and reach the lattice temperature within 5–10 ps. In contrast, with hot phonons, after the initial pulse, when a nonequilibrium distribution of hot

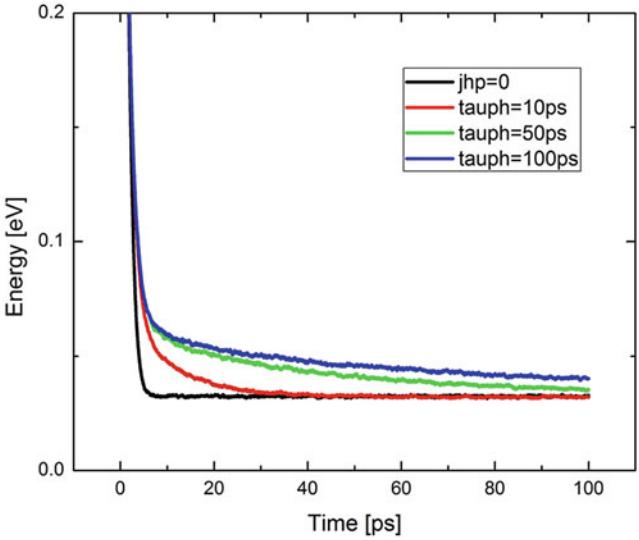

Fig. 1.21 Simulated electron temperature versus time for various assumed phonon lifetimes in a 10 nm GaAs/AlAs QW following a 2 eV, 200 fs wide optical pulse. The injected carrier density is 5×10^{11}/ cm^2 in all cases. The lattice temperature is 5 K

phonons establishes itself, the decay slows and becomes non-exponential. As expected, as the phonon decay time becomes very large, the energy loss rate transitions to one limited by the electron-phonon scattering time, to one determined by the phonon-phonon anharmonic decay time. Hence, finding absorber materials with long phonon lifetimes is a possible approach to realizing hot-carrier solar cell performance.

1.4 Summary

Here we have discussed the state of the art with respect to photovoltaic device technology and how nanotechnology is playing an increasing role in improving existing devices, as well as new device architectures seeking to improve efficiency while lower cost. We discussed how, for example, nanostructures are playing an increasing role in improving light management in solar cells to improve light collection and allow thinner materials to be used reducing cost. Nanostructured materials play a central role in device architectures such as the dye-sensitized solar cell, which in turn became the basis for perovskite solar cells, which have rapidly overtaken thin-film technology in terms of efficiency and approach that of crystalline Si solar cells. Nanowire solar cells have also shown tremendous improvement in recent years, with efficiencies over 15%. Research continues on realizing advanced concept solar cell structures such as multiexciton generation and hot-carrier solar cells, and recent results show continued improvement in the design and architectures of such systems.

References

1. Photovoltaics Report (PDF). Fraunhofer ISE. 12 July 2017
2. Yoshikaw K, Kawasaki H, Yoshida W, Irie T, Konishi K, Nakano K, Uto T, Adachi D, Kanematsu M, Uzu H, Yamamoto K (2017) Silicon heterojunction solar cell with interdigitated back contacts for a photoconversion efficiency over 26%. Nat Energy 2:1–8
3. https://www.altadevices.com/
4. "First solar builds the highest efficiency thin film PV cell on record". firstsolar.com
5. Dennler G, Scharber MC, Brabec CJ (2009) Polymer-fullerene bulk-heterojunction solar cells. Adv Mater 21:1323–1338
6. Timmreck R, Meyer T, Gilot J, Seifert H, Nueller T, Furlan A, Wienk MM, Wynands D, Hohl-Ebinger J, Warta W, Janssen RAJ, Riede M, Leo K (2015) Characterizaion of tandem organic solar cells. Nat Photonics 9:478–479
7. Grätzel M (2014) The light and shade of perovskite solar cells. Nat Mater 13:838–842
8. Kojima A, Teshima K, Shirai Y, Miyasaka T (2009) Organometal halide perovskites as visible-light sensitizers for photovoltaic cells. J Am Chem Soc 131:6050–6051
9. Liu M, Johnston MB, Snaith HJ (2013) Efficient planar heterojunction perovskite solar cells by vapour deposition. Nature 501:395–398
10. Shockley W, Queisser HJ (1961) Detailed balance limit of efficiency of p-n junction solar cells. J Appl Phys 32:510–519
11. de Vos A (1992) Endoreversible thermodynamics of solar energy conversion. Oxford University Press, Oxford
12. Kolodinski S, Werner JH, Wittchen T, Queisser HJ (1993) Quantum efficiencies exceeding unity due to impact ionization in silicon solar cells. Appl Phys Lett 63:2405
13. Schaller R, Klimov V (2004) High efficiency carrier multiplication in pbse nanocrystals: implications for solar energy conversion. Phys Rev Lett 92:186601
14. Ross RT, Nozik AJ (1982) Efficiency of hot-carrier solar energy converters. J Appl Phys 53:3813
15. Würfel P (1997) Solar energy conversion with hot electrons from impact ionization. Sol Energy Mater Sol Cells 46:43
16. Würfel P, Brown AS, Humphrey TE, Green MA (2005) Particle conservation in the hot-carrier solar cell. Prog Photovolt Res Appl 13:277
17. Cotal H, Fetzer C, Boisvert J, Kinsey G, King R, Hebert P, Yoon H, Karam N (2009) III–V multijunction solar cells for concentrating photovoltaics. Energy Environ Sci 2:174–192
18. Press Release, Fraunhofer Institute for Solar Energy Systems, 1 December 2014 (accessed at http://www.ise.fraunhofer.de/en/ press-and-media/press-releases/press-releases-2014/new-world-record-for-solar-cell -efficiency-at-46-percent on 7 December 2014). Soitec record
19. Zhang C, Kim Y, Faleev NN, Honsberg CB (2017) Improvement of GaP crystal quality and silicon bulk lifetime in GaP/Si heteroepitaxy. J Cryst Growth 475(1):83–87
20. Weyers M, Sato M, Ando H (1992) Red shift of photoluminescence and absorption in dilute GaAsN alloy layers. Jpn J Appl Phys 31(pt. 2, 7A):L853–L955
21. Luque A, Martí A (1997) Increasing the efficiency of ideal solar cells by photon induced transitions at intermediate levels. Phys Rev Lett 78:5014–5017
22. Binnig G, Rohrer H, Gerber C, Weibel E (1982) Surface studies by scanning tunneling microscopy. Phys Rev Lett 49:57–60
23. Cho AY, Arthur JR (1975) Molecular beam epitaxy. Prog Solid State Chem 10:157–191
24. Lu W, Lieber CM (2006) Semiconductor nanowires. J Phys D Appl Phys 39:R387
25. Samuelson L (2003) Self-forming nanoscale devices. Mater Today 6:22–31
26. Björk MT, Ohlsson BJ, Sass T, Persson AI, Thelander C, Magnusson MH, Deppert K, Wallenberg LR, Samuelson L (2002) One-dimensional steeplechase for electrons realized. Nano Lett 2:87–89
27. Björk MT, Ohlsson BJ, Thelander C, Persson AI, Deppert K, Wallenberg LR, Samuelson L (2002) Nanowire resonant tunneling diodes. Appl Phys Lett 81:4458–4460

28. Thelander C, Martensson T, Björk MT, Ohlsson BJ, Larsson MW, Wallenberg LR, Samuelson L (2003) Single-electron transistors in heterostructure nanowires. Appl Phys Lett 83:2052–2054
29. Fuhrer A, Fasth C, Samuelson L (2007) Single electron pumping in InAs nanowire double quantum dots. Appl Phys Lett 91:052109
30. Fuhrer A, Froberg LE, Pedersen JN, Larsson MW, Wacker A, Pistol ME, Samuelson L (2007) Few electron double quantum dots in InAs/InP nanowire heterostructures. Nano Lett 7:243–246
31. Björk MT, Fuhrer A, Hansen AE, Larsson MW, Fröberg LE, Samuelson L (2005) Tunable effective g factor in InAs nanowire quantum dots. Phys Rev B 72:201307
32. Chandra N, Tracy CJ, Cho J-H, Picraux ST, Hathwar R, Goodnick SM (2015) Vertically grown Ge nanowire Schottky diodes on Si and Ge substrates. J Appl Phys 118:024301–024307
33. Alivisatos AP (1996) Perspectives on the physical chemistry of semiconductor nanocrystals. J Phys Chem 100:13226–13239
34. Bimberg D, Grundmann M, Ledentsov NN (1999) Quantum dot heterostructures. Wiley, Chichester
35. Ban K-Y, Bremner SP, Liu G, Dahal SN, Dippo PC, Norman AG, Honsberg CB (2010) Use of a GaAsSb buffer layer for the formation of small, uniform, and dense InAs quantum dots. Appl Phys Lett 96:183101
36. O'Regan B, Grätzel M (1991) A low-cost, high-efficiency solar cell based on dye-sensitized colloidal TiO_2 films. Nature 353:737–740
37. Seok SI, Grätzel M, Park N-G (2018) Methodologies toward Highly Efficient Perovskite Solar Cells. Small 14:1704177
38. Yablonovitch E (1982) Statistical ray optics. J Opt Soc Am A 72:899–907
39. John S (1987) Strong localization of photons in certain disordered dielectric superlattices. Phys Rev Lett 58(23):2486–2489
40. Yablonovitch E (1987) Inhibited spontaneous emission in solid-state physics and electronics. Phys Rev Lett 58(20):2059–2062
41. Vulic N, Choi J-Y, Honsberg CB, Goodnick SM (2015) Silica nanosphere lithography defined light trapping structures for ultra-thin Si photovoltaics. MRS Proc 1770:31–36
42. Kelzenberg MD, Boettcher SW, Petykiewicz JA, Turner-Evans DB, Putnam MC, Warren EL, Spurgeon JM, Briggs RM, Lewis NS, Atwater HA (2010) Enhanced absorption and carrier collection in Si wire arrays for photovoltaic applications. Nat Mater Lett 9:239–244
43. Pillai S, Catchpole KR, Trupke T, Green MA (2007) Surface plasmon enhanced silicon solar cells. J Appl Phys 101(9):093105
44. Nakayama K, Tanabe K, Atwater HA (2008) Plasmonic nanoparticle enhanced light absorption in GaAs solar cells. Appl Phys Lett 93(12):121904
45. Tian B et al (2007) Coaxial silicon nanowires nanoelectronic power sources. Nature 449:889
46. Garnett EC, Peidong Y (2008) Silicon nanowire radial p-n junctions solar cells. J Am Chem Soc 130(29):9224–9225
47. Tang J, Huo Z, Brittman S, Gao H, Yang P (2011) Solution-processed core-shell nanowires for efficient photovoltaic cells. Nat Nanotechnol 6(9):568–572
48. Kempa TJ, Kim SK, Day RW, Park HG, Nocera DC, Lieber CM (2013) Facet-selective growth on nanowires yields multi-component nanostructures and photonic devices. J Am Chem Soc 135(49):18354–18357
49. Treu J, Stettner T, Watzinger M, Morkötter S, Döblinger M, Matich S, Saller K, Bichler M, Abstreiter G, Finley JJ, Stangle J, Koblmüller G (2015) Lattice-matched InGaAs-InAlAs core-shell nanowires with improved luminescence and photoresponse properties. Nano Lett 15 (5):3533–3540
50. Popescu B, Popescu D, Luppina P, Julian T, Koblmüller G, Lugli P, Goodnick S (2015) Modeling and simulation of InGaAs nanowire solar cells. In Proceedings of the IEEE International Conference on Nanotechnology, Rome, Italy, pp 728–231
51. Chuang C, Sedgwick FG, Chen R, Ko WS, Moewe M, Ng W, Tran T-TD, Chang-Hasnain C (2010) GaAs-based nanoneedle light emitting diode and avalanche photodiode monolithically integrated on a silicon substrate. Nano Lett 11(2):385–390

52. Chen R, Tran T-TD, Ng KW, Ko WS, Chuang LC, Sedgwick FG, Chang-Hasnain C (2011) Nanolasers grown on silicon. Nat Photonics 5(3):170–175
53. Colombo C, Heiss M, Gratzel M, Fontcuberta I Morral A (2009) Gallium arsenide pin radial structures for photovoltaic applications. Appl Phys Lett 94(17):173108
54. Krogstrup P et al (2013) Single-nanowire solar cells beyond the Shockley-Queisser limit. Nat Photonics 7(4):206–310
55. Mariani G et al (2011) Patterned radial GaAs nanopillar solar cells. Nano Lett 11(6):2490–2494
56. Wallentin J, Anttu N, Asoli D, Huffman M, Magnusson IAMH, Siefer G, Fuss-Kailuweit P, Dimroth F, Witzigmann B, Xu HQ, Samuelson L, Deppert K, Borgström MT (2013) InP nanowire array solar cells achieving 13.8% efficiency by exceeding the ray optics limit. Science 339(6123):1057–1060
57. Åberg I, Vescovi G, Asoli D, Naseem U, Gilboy JP, Sundvall C, Dahlgren A, Svensson KE, Anttu N, Björk MT, Samuelson L (2016) A GaAs nanowire array solar cell with 15.3% efficiency at 1 sun. IEEE J Photovolt 6(1):185–190
58. van Dam D, van Hoof NJJ, Cui Y, van Veldhovern PJ, Bakkers EPAM, Rivas JG, Haverkort JEM (2016) High-efficiency nanowire solar cells with omnidirectionally enhanced absorption due to self aligned indium−tin−oxide mie scatterers. ACS Nano 10:11414–11419
59. Schaller RD, Klimov VI (2004) High efficiency carrier multiplication in PbSe nanocrystals: implications for solar energy conversion. Phys Rev Lett 92(18):186601
60. Ellingson RJ, Beard MC, Johnson JC, Yu P, Micic OI, Nozik AJ, Shabaev A, Efros AL (2005) Highly efficient multiple exciton generation in colloidal PbSe and PbS quantum dots. Nano Lett 5(5):865–871
61. Nozick AJ (2005) Exciton multiplication and relaxation dynamics in quantum dots: applications to ultrahigh-efficiency solar photon conversion. Inorganic Chem 44:6893
62. Shabaev A, Efros AL, Nozik AJ (2006) Multiexciton generation by a single photon in nanocrystals. Nano Lett 6:8
63. Schaller RD, Pietryga JM, Klimov VI (2007) Carrier multiplication in InAs nanocrystal quantum dots with an onset defined by the energy conservation limit. Nano Lett 7 (11):3469–3476
64. Murphy JE, Beard MC, Norman AG, Phillip S, Johnson JCA, Pingrong M, Olga IY, Ellingson RJ, Nozik AJ (2006) PbTe colloidal nanocrystals: synthesis, characterization, and multiple exciton generation. J Am Chem Soc 128(10):3241–3247
65. Werner JH, Kolodinski S, Queisser HJ (1994) Novel optimization principles and efficiency limits for semiconductor solar cells. Phys Rev Lett 72(24):3851–3854
66. Beard MC, Knutsen KP, Yu P, Luther JM, Song Q, Metzger WK, Ellingson RJ, Nozik AJ (2007) Multiple exciton generation in colloidal silicon nanocrystals. Nano Lett 7(8):2506–2512
67. Vos A d, Desoete B (1998) On the ideal performance of solar cells with larger-than-unity quantum efficiency. Sol Energy Mater Sol Cells 51(3):413–424
68. Semonin OE, Luther JM, Choi S, Chen H-Y, Gao J, Nozik AJ, Beard MC (2012) Peak external photocurrent quantum efficiency exceeding 100% via MEG in a quantum dot solar cell. Science 334:1530–1533
69. Cunningham PD, Boercker JE, Foos EE, Lumb MP, Smith AR, Tischler JG, Melinger JS (2011) Enhanced multiple exciton generation in quasi-one-dimensional semiconductors. Nano Lett 11 (8):3476–3481
70. Hathwar R, Saraniti M, Goodnick SM (2015) Energy relaxation and non-linear transport in InAs nanowires. J Phys Conf Ser 647:012039
71. Ross RT, Nozik AJ (1982) Efficiency of hot-carrier solar energy converters. J Appl Phys 53:3813–3818
72. Landsberg PT, Tonge G (1980) Thermodynamic energy conversion efficiencies. J Appl Phys 51:R1
73. Würfel P (1997) Solar energy conversion with hot electrons from impact ionization. Sol Energy Mater Sol Cells 46:43–52

74. Würfel P, Brown AS, Humphrey TE, Green MA (2005) Particle conservation in the hot-carrier solar cell. Prog Photovolt Res Appl 13:277
75. Conibeer G, Green MA, Corkish R, Cho Y, Chob E, Jiang C, Fangsuwannarak T, Pink E, Huang Y, Puzzer T, Trupke T, Richards B, Shalav A, Lind K (2006) Silicon nanostructures for third generation photovoltaic solar cells. Thin Solid Films 511–512:654
76. Pelouch WS, Ellingson RJ, Powers PE, Tang CL, Szmyd DM, Nozik AJ (1992) Comparison of hot-carrier relaxation in quantum wells and bulk GaAs at high carrier densities. Phys Rev B 45:1450–1453
77. Tsen KS, Wald KR, Ruf T, Yu PY, Morkoc H (1991) Electron optical phonon interactions in ultrathin GaAs AlAs multiple quantum well structures. Phys Rev Lett 67:2557–2560
78. Tsen KT, Joshi RP, Ferry DK, Botcharev A, Sverdlov B, Salvador A, Morkoc H (1996) Non-equilibrium electron distributions and phonon dynamics in wurtzite GaN. Appl Phys Lett 68:2990–2992
79. Tsen KT, Kiang JG, Ferry DK, Morkoc H (2006) Subpicosecond time-resolved Raman studies of LO phonons in GaN: dependence on photoexcited carrier density. Appl Phys Lett 89:112111
80. Tsen KT, Kiang JG, Ferry DK, Lu H, Schaff WJ, Lin H-W, Gwo S (2007) Direct measurements of the lifetimes of longitudinal optical phonon modes and their dynamics in InN. *Appl Phys Lett* 90:152107-1-3
81. Goodnick SM, Lugli P (1992) Hot carrier relaxation in quasi-2D systems. In: Shah J (ed) Hot carriers in semiconductor microstructures: physics and applications. Academic Press, New York, pp 191–234
82. Dür M, Goodnick SM, Lugli P (1996) Monte Carlo simulation of intersubband relaxation in wide, uniformly doped GaAs/AlxGa1-xAs quantum wells. *Phys Rev B* 54:17794
83. Conibeer G, Patterson R, Huang L, Guillemoles J-F, König D, Shrestha S, Green MA (2010) Modelling of hot carrier solar cell absorbers. Sol Energy Mater Sol Cells 94:1516–1521
84. Goodnick SM, Honsberg C (2012) Modeling carrier relaxation in hot carrier solar cells. *Proc SPIE* 8256:82560W. https://doi.org/10.1117/12.910858